communications earth & environment

Article

https://doi.org/10.1038/s43247-024-01636-9

Global increase in the optimal temperature for the productivity of terrestrial ecosystems

Zhongxiang Fang[1], Wenmin Zhang[1] ✉, Lanhui Wang[2,3], Guy Schurgers[1], Philippe Ciais[4], Josep Peñuelas[5], Martin Brandt[1], Hui Yang[6], Ke Huang[1], Qiu Shen[7] & Fensholt Rasmus[1]

Vegetation growth may adapt to climate warming by adjusting the relationship between photosynthetic capacity and temperature. However, changes in the optimal temperature for ecosystem productivity during recent decades of warming remain uncertain. Here we provide empirical evidence that global optimal temperature increased at a rate of 0.017 ± 0.002 °C y^{-1} from 1982 to 2016, using multiple datasets of satellite-derived productivity and climate variables. Model simulations show that the optimal temperature will increase by 0.027 ± 0.001 °C y^{-1} until the end of 21st century. The global increasing optimal temperature is consistent with increasing mean air temperatures and model simulations further confirm the key role of temperature in regulating changes in optimal temperature, while being co-regulated by other factors, such as CO_2 and precipitation. These results suggest that vegetation is acclimating to warming and that the negative impacts of climate change on ecosystem productivity may be less severe than previously thought.

Photosynthesis in global terrestrial ecosystems is a key driver of the land carbon sink, which removes 30% of CO_2 from anthropogenic emissions of carbon[1]. The capacity of global photosynthesis to fix atmospheric CO_2 depends on temperature, water and many other factors (e.g., nutrients and VPD)[2,3]. Under controlled conditions, leaf-scale photosynthesis first increases with warming until a maximum rate is reached defining an optimum temperature (T_{opt}), after which it decreases with additional warming[4–6]. T_{opt} is linked to the maximum gross primary productivity (GPP) of terrestrial ecosystems[7] and represents an essential ecophysiological variable for modeling the global interactions between the terrestrial biosphere and the atmosphere[8].

Differences in T_{opt} across ecosystems, inferred from in situ flux observations, have been documented[9] and many studies have reported that T_{opt} is closely associated with the mean air temperature of a region[8,10]. For example, vegetation T_{opt} is found to be higher in warmer areas as compared to cold regions[6]; a phenomenon suggesting long-term thermal adaptation. Whether T_{opt} potentially can change over time as a consequence of the observed increase in temperature during the recent decades[11] however remains unproven. Changes in the availability of water or nutrients[12], CO_2 levels[10], and land cover[13] may regulate the relationship between increasing temperatures and vegetation photosynthesis, which could cause temporal changes in T_{opt}. These lines of evidence support the hypothesis that temporal changes in T_{opt} of photosynthesis might potentially occur in a warming climate[14]. If T_{opt} is increasing around the globe, it may support a continued increase of the global vegetation carbon sink[15] rather than slowing down or reversing under the warming world[16,17]. Studying temporal changes in T_{opt} at the global scale is therefore pivotal to better understand the response of the global carbon cycle to global warming[18].

We define T_{opt} as the monthly mean temperature at which GPP is highest within a given spatiotemporal "window" (5 years temporal window and 10 × 10 pixels of spatial window). Using multiple satellite-derived estimates for GPP and reanalysis climatic data sets, we first estimate the temporal dynamics of ecosystem T_{opt} at the global scale during the period 1982 to 2016. We then study potential forcing variables of the changing T_{opt} and attempt a coarse extrapolation of potential changes in T_{opt} for 2017–2100 using the outputs of Coupled Model Intercomparison Project Phase 6 (CMIP6) under various climatic scenarios.

[1]Department of Geosciences and Natural Resource Management, University of Copenhagen, Øster Voldgade 10, DK-1350 Copenhagen, Denmark. [2]Center for Biodiversity Dynamics in a Changing World (BIOCHANGE) and Section for Ecoinformatics & Biodiversity, Department of Biology, Aarhus University, Ny Munkegade 114, 8000 Aarhus C, Denmark. [3]Department of Physical Geography and Ecosystem Science, Lund University, Sölvegatan 12, SE- 223 62, Lund, Sweden. [4]Laboratoire des Sciences du Climat et de l'Environnement, CEA CNRS UVSQ, Gif-sur-Yvette, France. [5]CSIC, Global Ecology Unit CREAF-CEAB-UAB, Cerdanyola del Vallès, 08193 Catalonia, Spain. [6]Department for Biogeochemical Integration, Max-Planck-Institute for Biogeochemistry, 07745 Jena, Germany. [7]Faculty of Geographical Science, Beijing Normal University, Beijing, 100875, China. ✉e-mail: wenminzhg@gmail.com

Results

Global increase in T_{opt}

Changes in T_{opt} are detected using a 5-year temporal moving window and a 1° spatial window (Supplementary Fig. 1) with multiple satellite-based products of GPP proxies (NIR GPP, KNDVI, NDVI, EVI) that are independent on climate variables as input (see Methods and Supplementary Table 1). The results indicate that the global average T_{opt} based on NIR GPP has significantly ($p < 0.05$) increased from 18.64 ± 5.0 (mean ± std) to 19.18 ± 5.1 °C, with an average rate of 0.017 ± 0.002 °C y^{-1} (Fig. 1A) over the last 35 years. The increase in T_{opt} was supported by increasing T_{opt} derived from other temperature independent GPP proxies (KNDVI, NDVI and EVI). The majority of grid cells (69.6%) have a higher T_{opt} in the period 2012-2016 than in the period 1982–1986 (Fig. 1B). A higher T_{opt} in the later period (2010–2014) than in the earlier period (2001–2005) was also observed for most sites included in FLUXNET (Supplementary Fig. 2). Moreover, increases in T_{opt} are found with different spatiotemporal windows (Supplementary Fig. 3), different combinations of GPP and temperature data sets (Supplementary Fig. 4), different temporal composition of GPP data sets (Supplementary Fig. 5), a larger body of different vegetation productivity proxy products (Supplementary Figs. 6, 7), different temperature data sets (Supplementary Fig. 8), and different methods used to smooth the response curve of vegetation productivity to temperature (Supplementary Fig. 9), demonstrating the robustness of the observed patterns.

The spatial patterns of the temporal trend of increasing T_{opt} indicate that T_{opt} significantly ($p < 0.05$) increased over 22.6% of the global terrestrial ecosystems (Fig. 1C), whereas a significantly ($p < 0.05$) negative trend in T_{opt} is observed only for 6.0% of the global terrestrial ecosystems, mainly in western Siberia, savannas, and grasslands in northern Australia and southern Africa. The increase in T_{opt} is closely associated with the increase in temperature from 1982 to 2016, both at the global scale and for different climatic zones (Supplementary Fig. 10). Globally, T_{opt} is lower than the 80th percentile of temperature (Supplementary Fig. 10), indicating that T_{opt} is generally lower than extreme warm air temperatures. The difference between T_{opt} and the upper air temperature percentiles is particularly pronounced in tropical zone, where T_{opt} is much lower than the 50% temperature percentiles. In contrast, T_{opt} generally exceeds the 90th percentile of temperature in the polar zone (Supplementary Fig. 10), indicating that air temperature is markedly lower than T_{opt} in this biome.

Drivers of increasing T_{opt}

The complex co-regulation of various climatic factors to vegetation growth makes it challenging to derive contributions of these factors to vegetation change solely based on earth observation data. We thus used monthly GPP data sets simulated by process-based dynamic global vegetation models coupled by "Trends and drivers of the regional scale sources and sinks of carbon dioxide" (TRENDY, version 9) under four scenarios (S0, S1, S2, and S3, see Methods and Supplementary Table 2) to investigate the relative importance of drivers controlling changes in T_{opt}. A good agreement between satellite and modelling derived T_{opt} under the standard scenario (S3) reinforces confidence in the modelling simulations (Supplementary Fig. 11). We used the TRENDY modelling simulations to identify the forcing variables driving the increasing T_{opt}, by comparing the differences between the trend in T_{opt} from S3 and other simulations (see Methods and Supplementary Table 2). Globally, the simulation driven only by climate (CL) shows a T_{opt} trend much closer to the standard scenario (S3, $CO_2 + CL + LC$) than trends under scenarios that are driven only by either CO_2 or LC (Fig. 2A), suggesting that climate change plays the most important role in controlling increasing T_{opt}. The contribution of individual climate factors (e.g., temperature, precipitation, and radiation) cannot be differentiated due to the combined use of climate variables as input for the TRENDY models. However, the simulations from the LPJ-GUESS model allow to study the impact of individual climate forcing variables on T_{opt} (Fig. 2B).

Similar to the simulations of TRENDY, we show a good agreement in T_{opt} estimates based on satellite observations and the LPJ-GUESS model to support the validity of modelling simulations of T_{opt} (Supplementary Fig. 12 and Supplementary Table 3). The simulation driven by varying temperature

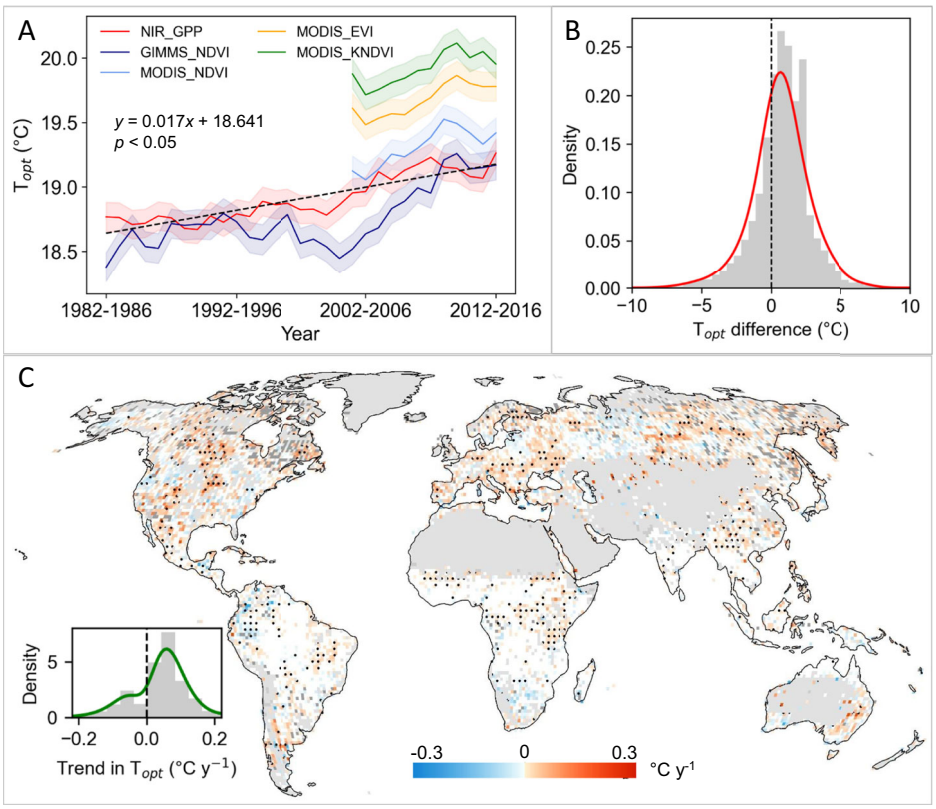

Fig. 1 | Global increase in T_{opt} of ecosystem photosynthesis. A Temporal dynamics of T_{opt} for four GPP data sets with a 5-y temporal window and a 1° spatial window for 1982–2016. The solid lines indicate the dynamics of T_{opt}, and the shaded areas represent the 95% confidence interval of T_{opt}. The dashed black line indicates the trend in T_{opt} based on the NIR GPP data set. **B** Histogram of the difference in T_{opt} between the first period (1982–1986) and the last period (2012–2016) for all 1° grids ($n = 7971$) derived from the NIR GPP data sets. The density function represents the standardized frequency (the sum of the area between x-axis and density function is 1). **C** Spatial patterns of trends in T_{opt} derived from the NIR GPP data sets using a 5-y temporal window and a 1° spatial window for 1982–2016. The black points denote significant trends ($p < 0.05$). Dark gray indicates areas where T_{opt} could not be successfully retrieved (see Methods, Supplementary Fig. 1d) for more than 40% of the temporal windows considered, and light gray indicates irrigated cropland and areas with sparse or no vegetation.

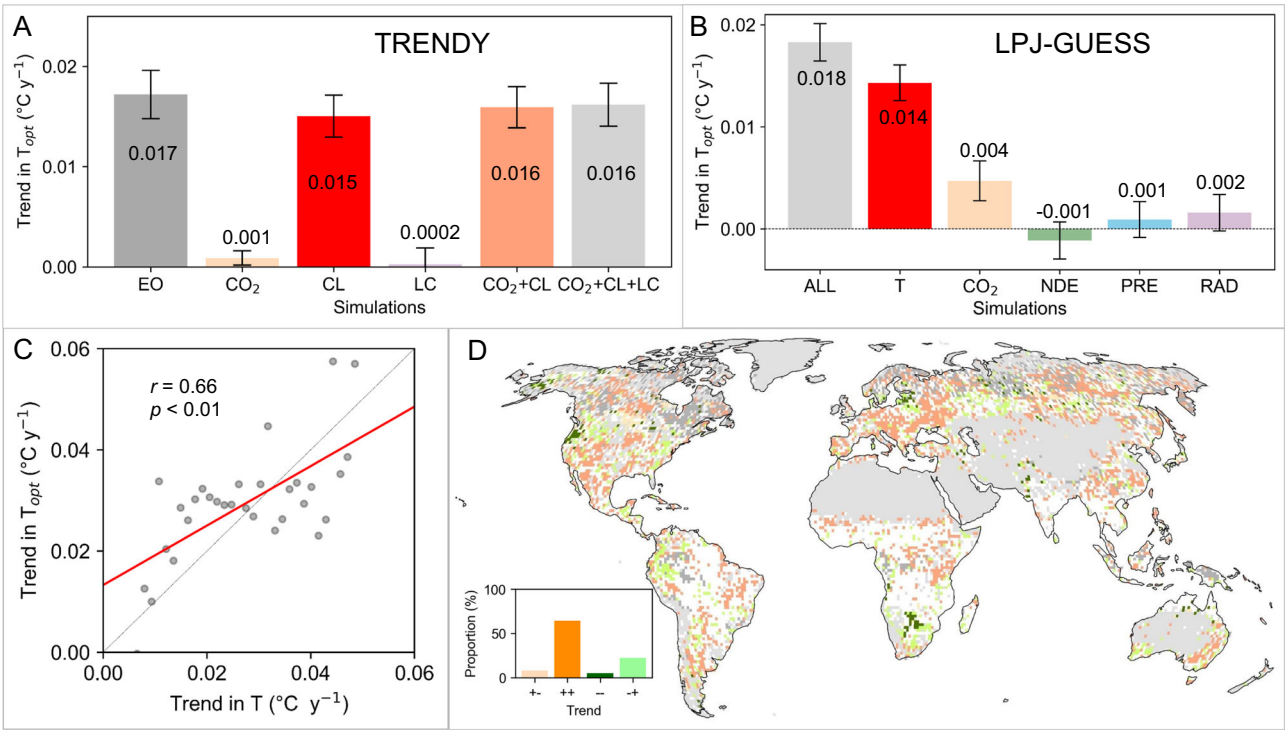

Fig. 2 | Forcing variables of changes in T_{opt}. **A** Trends in T_{opt} from Earth observation data (EO) and from multi-model mean (TRENDY) of dynamic global vegetation models under different conditions: driven by varying CO_2 only (CO_2), driven by climate change only (CL), driven by land cover change only (LC), driven by varying CO_2 and climate change (CO_2 + CL), and driven by all above factors (CO_2 + CL + LC) varying. The numbers superimposed on the bars denote the magnitude of trends in Topt under the different scenarios. **B** Trends in T_{opt} from the LPJ-GUESS model under different conditions: driven by all factors varying (ALL), driven by varying temperature only (T), driven by varying CO_2 only (CO_2), driven by varying nitrogen deposition only (NDE), driven by varying precipitation only (PRE), and driven by varying solar radiation only (RAD). The numbers superimposed on the bars denote the magnitude of trends in T_{opt} under the different scenarios. The error bars indicate 95% confidence interval of trends in T_{opt}. **C** The relationship between the trend in satellite-observed T_{opt} and the trend in a 5-y moving window of mean air temperature derived from the ERA5 data set for 1982–2016. **D** The consistency between the trend in satellite-observed T_{opt} and the trend in the 5-y moving window of mean air temperature derived from the ERA5 data set. +-, increasing T_{opt} and decreasing T; ++, increasing T_{opt} and increasing T; --, decreasing T_{opt} and decreasing T; -+, decreasing T_{opt} and increasing T; n = 5323. Gray indicates irrigated cropland and areas with sparse or no vegetation.

only (T) shows the highest increasing trend in T_{opt}, which is more similar to the simulation under standard conditions, compared with trends in T_{opt} under other simulations with a varying CO_2 level only (CO_2), varying nitrogen deposition only (NDE), varying precipitation only (PRE), and varying solar radiation only (RAD) (Fig. 2B). The modelling results obtained from these factorial simulations thereby suggest that air temperature is the most important climate factor for changes in T_{opt}, followed by CO_2 level and solar radiation. Furthermore, satellite observations also show that changes in temperature has the largest relative importance (71.12%) for the changes in T_{opt} (Supplementary Fig. 13).

We also evaluate the relationship between satellite-observed T_{opt} and its main climatic driver (air temperature). The trend in air temperature is binned into 100 groups, and the mean trend in T_{opt} in each group is derived. The trend in satellite-observed T_{opt} is significantly positively correlated (r = 0.66, p < 0.01) with the trend in mean air temperature in a 5-y moving window derived from the ERA5 data set (Fig. 2C). The trends in T_{opt} and mean air temperature are consistent in most areas around the world, accounting for 65.1% of the area under analysis, with 64.5% of the area indicating consistently positive trends (++) and 0.06% indicating negative trends (--) (Fig. 2C). The trends in T_{opt} and temperature (+- or -+) are found to be inconsistent in scattered regions in western Siberia, eastern China, and south-central Africa, totaling an area of 34.9%. As compared to the consistency found between T_{opt} and temperature, the majority of pixels (57.5%) showed inconsistency (+- or -+) between trends in T_{opt} and trends in precipitation (Supplementary Fig. 14) also supporting the key importance of temperature as a driver of the observed trends in T_{opt}.

Projected changes in T_{opt}

Projected changes in T_{opt} and its relationship with increasing future air temperatures are estimated by deriving the multi-model mean historical and projected T_{opt} from 23 CMIP6 models. We first compare the consistency between T_{opt} derived from the historical CMIP6 models and from satellite observations (NIR GPP) using a 5-y temporal window and a 5° spatial window, which showed a good agreement (Supplementary Fig. 15). Similarly, the trends in T_{opt}, the monthly mean temperature, and monthly maximum temperature derived from CMIP6 models are simulated (Fig. 3A) under scenarios of future climate (Supplementary Fig. 16). T_{opt} under the SSP245 scenario increased at a rate of 0.027 ± 0.001 °C y^{-1}, which is higher than the increases in monthly mean temperature (0.022 ± 0.001 °C y^{-1}), but lower than the increases in monthly maximum temperature (0.035 ± 0.001 °C y^{-1}) (Fig. 3A, Supplementary Fig. 16). This finding suggests that vegetation is adapting to future climatic warming but cannot match the rate of maximum warming. The projected increases in T_{opt} are likely to slow down (Supplementary Figs. 16, 17), following the decrease in the level of emissions from SSP585 to SSP126, or even halt (SSP126) after 2050. A global increase in T_{opt} in the last 5-y period (2096–2100) is evident under all scenarios, especially for SSP585, compared to the first 5-y period (2017-2021). Overall, under the SSP245 scenario, higher latitudes will have larger increase in T_{opt}, matching a greater degree of warming in the future. Specifically, polar and cold areas are expected to have the largest increases in T_{opt} (2.08 and 2.28 °C), together with the highest increase in monthly maximum temperature (2.89 and 2.97 °C)), but lowest monthly mean temperature (1.50 and 1.79 °C). Temperate and arid areas will have the smallest increase in T_{opt} (1.85 and 1.89 °C), together with lower increase in

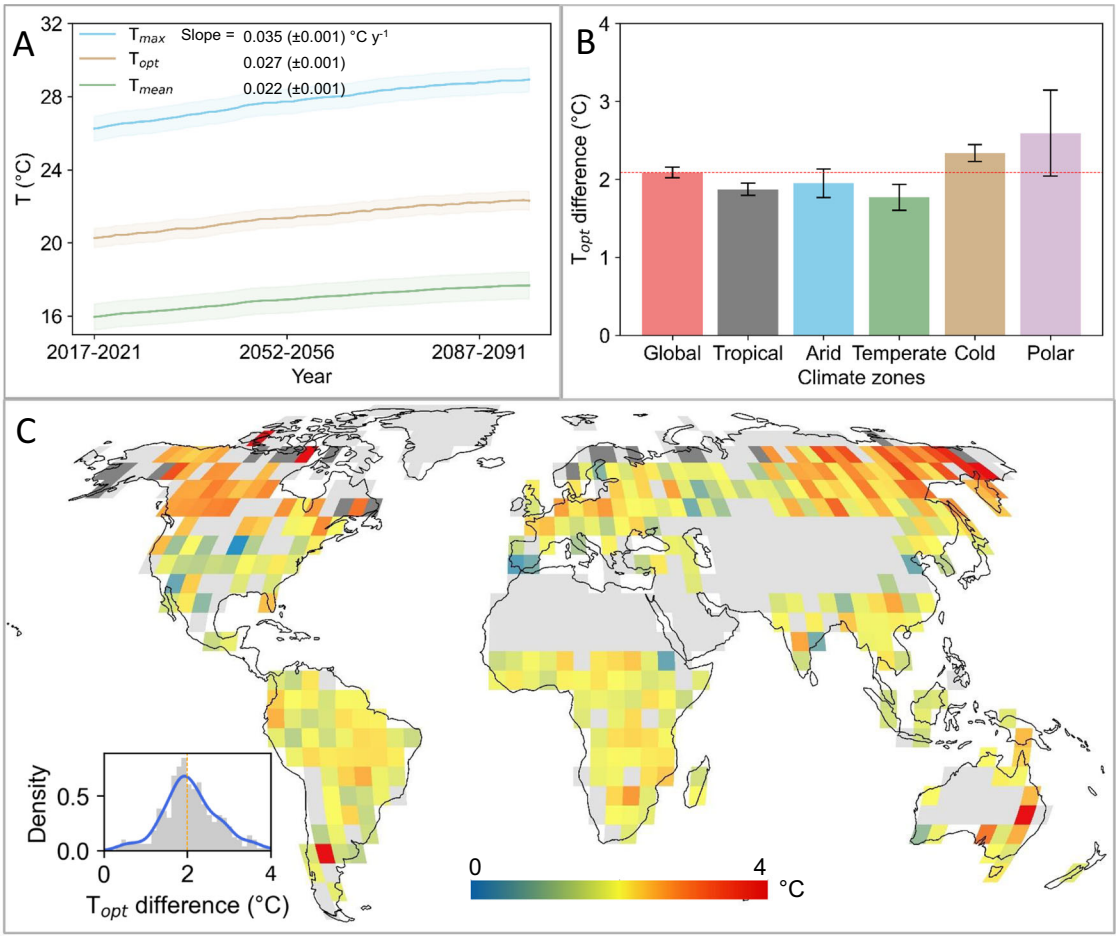

Fig. 3 | Projected changes in T_{opt} of ecosystem productivity under the SSP245 scenario. A Projected temporal change of T_{opt}, monthly maximum temperature, and monthly mean temperature for 2017–2100. T_{opt} is estimated from 23 CMIP6 models with a 5-y temporal window and a 5° spatial window for 2017–2100. The maximum and mean temperatures are calculated using the same spatio-temporal windows as for T_{opt}. The solid lines indicate the dynamics of T_{opt}, maximum temperature, and mean temperature, and the shaded areas represent the 95% confidence interval of the maximum temperature, optimal temperature, and mean temperature. **B** The difference in mean T_{opt} of two 5-y periods, 2017–2021 and 2096–2100, under the SSP245 scenario at the global scale and for different climatic zones. The error bars indicate 95% confidence interval of the difference in T_{opt}. **C** Spatial patterns of the difference in T_{opt} between two periods (2017–2021 and 2096–2100) under the SSP245 scenario. Gray indicates irrigated cropland and areas with sparse or no vegetation. Dark gray pixels indicate areas with T_{opt} successfully extracted by less than 15 models.

monthly maximum temperature (2.46 and 2.46 °C) but quite large monthly mean temperature (1.94 and 1.98 °C). Tropical areas face moderate increases in T_{opt} (2.0 °C) (Fig. 3B, C), together with moderate increase in monthly maximum temperature (2.48 °C) but largest monthly mean temperature (2.10 °C) (Supplementary Fig. 16).

Discussion

Our study shows a global increase in T_{opt} of ecosystem photosynthesis over the last four decades, which suggests an acclimation of terrestrial ecosystems to increasing temperatures under global warming. We further demonstrate that increasing temperatures are the key driver for the increasing T_{opt}. This finding is partly supported by a local-scale study[19]. Spatial variations in the increase of T_{opt} are also evident, showing a substantially lower T_{opt} in colder areas compared to warmer areas[6]. Moreover, the increase in T_{opt} is not uniform across space, with a higher increase in T_{opt} in cold and arctic areas, which is likely related to the rapid warming in the northern high latitudes (arctic warming)[20]. An increase in temperature can affect T_{opt} in different ways: Firstly, at the leaf level, changes in temperature can regulate photosynthetic Rubisco activity and electron transport, which is the principal mechanism controlling photosynthesis[11]. The capacity of electron transport and/or the thermal stability of Rubisco can therefore determine the acclimation of vegetation photosynthesis to increasing temperature[21]. However, our paper mainly focuses on the changes in T_{opt} at ecosystem level based on satellite observations and model simulations (no long term thermal acclimation included in the models). We acknowledge that it cannot be inferred from this analysis whether the above mentioned thermal acclimation occurred at leaf level globally or not, although field observations already showed thermal acclimation at ground level in many different regions[8,9,19]. Secondly, higher temperatures induced higher vapor-pressure deficits (VPD, a proxy of atmospheric aridity)[22] could lead to stomatal closure to reduce the loss of water at the cost of a decrease in CO_2 exchange (productivity)[23], which may increase vegetation resistance to increasing temperatures. However, at the ecosystem level, increasing temperatures may drive changes in vegetation composition or lead to species adapting to higher temperature tolerance, which could contribute to the T_{opt} increases. This is particularly evident in the Northern hemisphere, woody encroaching into tundra biome due to climate warming[24,25], which probably increase T_{opt}.

Other factors (e.g. precipitation and CO_2 level) also affect T_{opt} (Fig. 2A) by altering the relationship between vegetation productivity and temperature. Firstly, the responses of T_{opt} to climatic variables can be affected by water availability, especially in water-limited areas, where the extent to which precipitation and solar radiation exerts control on T_{opt}, are largely dependent on dryness conditions[12]. This is likely attributed to the arid conditions that result in water scarcity within the soil, limiting vegetation's

ability to uptake water causing plants to close their stomata to mitigate water loss[26], consequently reducing photosynthesis. Moreover, dryness can increase the risks of dehydration and heat stress, reducing photosynthesis[27]. Elevated CO_2 could promote increase in T_{opt} for plant growth by enhancing photosynthetic efficiency, improving water and nutrient use, and thereby enabling better thermal tolerance[21,28,29]. However, a few areas showed significantly decreasing T_{opt}, such as southern Africa, western North America, and the northwestern Amazon rainforest. The decrease in southern Africa and western North America could be related to a regional cooling trend in these areas (Fig. 2D), while the decrease in the northwestern Amazon rainforest could be related low quality of the optical satellite dataset in this region due to cloud cover[30].

A globally increasing T_{opt} can have important implications for how terrestrial ecosystems are studied and for their functioning. Firstly, some studies have assumed that T_{opt} is constant[10], which is expected to be breached by the increasing temperatures in the foreseeable future[31]. The continuation of increasing temperatures would then be expected to have increasingly adverse impacts on ecosystems[4]. Our results, however, suggest thermal acclimation of ecosystems to increasing temperatures, which could to some extent delay the adverse effects as compared to what is currently expected[31]. Specifically, acclimation of global ecosystem photosynthesis to the increasing temperature implies that global warming will have less negative impacts on ecosystem productivity, which may eventually lead to a longer period of greening trend (carbon uptake) in the future than previously thought. For example, assuming a constant T_{opt}, Zhang et al.[31] reported a much earlier future point in time when summer temperatures would exceed T_{opt} under future warming scenarios than the point in time when the temperature would negatively affect ecosystem GPP under all scenarios of future emissions, which could be partially attributed to neglecting thermal acclimation. Secondly, the acclimation of ecosystems to increasing temperatures could account for the decrease in the relative contribution of temperature to vegetation productivity[32]. Lastly, ecosystem acclimation also indicates the increase of heat tolerance of global ecosystems by adjusting their traits and physiological processes (e.g., modifying their phenology, growth patterns, and metabolic functions) in response to changing environmental conditions, which would allow ecosystems to better cope with extreme climate events.

A recent study however shows insignificant changes in ecosystem-scale T_{opt} during recent decades[6], which is different from our results. We have looked into this apparent discrepancy and have found that the difference may be attributed to the several reasons: Firstly, Huang, et al.[6] used observations from a 10-year temporal window without including a spatial window[10], which could lead to insufficient observations for the extraction of T_{opt} (Supplementary Figs. 18, 19) thereby creating larger uncertainty in the T_{opt} assessment ultimately concealing subtle trends. Secondly, the results reported by Huang, et al. [6] were based on the monthly mean of daily maximum temperatures ($\mathbf{T}_{opt}^{max}$), while we use the monthly mean of daily mean temperatures. Therefore, we examined the changes in T_{opt} using both $\mathbf{T}_{opt}^{max}$ and the monthly mean of daily mean temperatures ($\mathbf{T}_{opt}^{mean}$) and found that both of them produced globally increasing trends, and both trends are highly consistent (Supplementary Fig. 20). This suggests that different temperature metrics have little impact on the globally increasing trends in T_{opt}. Thirdly, based on our method, we also use the same NDVI data set (used in Huang's paper) to estimate T_{opt} from 1982 to 2016 (Supplementary Fig. 6c). Trends in T_{opt} derived from these data sets are generally consistent, which also suggests a globally increasing trends in T_{opt}. Lastly, we use a fitting method of the Savitzky-Golay filter to fit 90% of GPP as a function of temperature, where T_{opt} is extracted at a point of maximum GPP. This fitting approach makes the output less sensitive to noise in the original GPP, which is considered an advantage over the direct use of the maximum of 90% of GPP to calculate T_{opt} applied in the previous study.

Our findings may be subject to some limitations. Firstly, good agreements of trends in T_{opt} derived from different vegetation proxies were found across global regions, except for tropical rainforests (Supplementary Figs. 3–6). This may be caused by the relatively poor data quality of the original AVHRR satellite data due to cloud cover and signal saturation of NDVI in these tropical areas[30]. Secondly, to extract T_{opt}, we used cubic convolution interpolation to resample the GPP data sets to 0.1° to match the spatial resolution of the climate data sets, which may introduce bias in areas characterized by high spatial variability. Thirdly, we used spatial windows to obtain sufficient observations to extract T_{opt}. However, the window size could affect the extraction of T_{opt} because plant function type within different size of windows may different, especially in the areas with high spatial variability. However, we found similar spatial patterns of T_{opt} trend, using different sizes of spatial, suggesting the limited impacts of varying size of moving window on the T_{opt}. Lastly, our study shows that global ecosystem T_{opt} will continue to increase under global warming. However, these results are mainly derived from CMIP6 model simulations, which rely on the response equations of ecosystem photosynthesis to climate factors and human emissions. These results should be interpreted with caution, particularly under the climate scenario of SSP585, because thermal acclimation extending beyond 37 °C is uncertain[11].

Our study document a widespread increase in T_{opt} at the global scale, but we cannot yet provide a detailed answer to whether the changes in T_{opt} over the last four decades are due to long-term genetic adaptation of the vegetation or to a short-term physiological response of the vegetation to climate change. More studies conducted at the species level[9,19] are needed to resolve this question. Our study only involves changes in the optimal temperature of photosynthesis, and further research should also be targeted towards exploring the changes in T_{opt} for ecosystem respiration and net ecosystem productivity and their inflection points under a projected warming world[33]. These studies will be critical for deepening our understanding of the exchange of carbon and energy in terrestrial ecosystems with implications for current efforts in achieving carbon neutrality.

Methods

GPP proxy data sets

Many studies have suggested that Near-infrared reflectance (NIR) has high correlations with GPP and it is at the same time less sensitive to non-vegetation objects in most ecosystems[34]. We therefore used a monthly GPP data set to estimate T_{opt}, derived from satellite-based NIR, covering the period from 1982 to 2018 with a spatial resolution of 0.05°[35]. NIR GPP is generated independent on climate variables as input for the calculation of the product. Furthermore, to test the robustness of our results we also used four other data sets that are independent on temperature data sets to extract T_{opt}. This involved the use data sets from vegetation indices including 3rd generation of Global Inventory Monitoring and Modeling System (GIMMS 3 g) normalized difference vegetation index (NDVI)[36], 4th generation leaf area index (LAI) (GIMMS LAI4g)[37], the MODIS NDVI, the MODIS enhanced vegetation index (EVI) and MODIS kernel NDVI (KNDVI)[38] representing two different types of satellite sensor systems. The GIMMS NDVI data set represents the longest continuous time series of vegetation indices, covering from 1982 to 2016 with a 15-d temporal resolution and 1/12° spatial resolution. The GIMMS LAI4g share the same spatial and temporal resolution with GIMMS NDVI, but covers from 1982 to 2015. The monthly MODIS NDVI, and EVI data sets (MOD13C2) cover from 2001 to 2016 with 0.05° spatial resolution. Monthly MODIS KNDVI is produced from MOD13C2 red and NIR reflectance from 2001 to 2016[38]. KNDVI is a nonlinear NDVI designed to have a higher sensitivity to vegetation biophysical and physiological processes, and thus is reported to have a more accurate estimation of terrestrial photosynthesis[38].

In addition, five other data sets were used to test the robustness of the estimation of T_{opt}, but were kept here secondary data sets, as these to some extent make use of temperature information in the modelling of GPP, that could potentially cause spurious co-varying trends with T_{opt}: Improved (light use efficiency) LUE GPP[39], Global Land Surface Satellite (GLASS) GPP[40], solar-induced chlorophyll fluorescence (SIF) GPP (GOSIF GPP)[41], spatial contiguous SIF (CSIF)[42], FLUXCOM GPP[43], and FLUXSAT GPP data sets. The Improved LUE GPP data set is based on the Monteith's LUE approach. The equation applied is improved with optimized spatiotemporal

LUEs, GIMMS3g of the canopy fraction of photosynthetically active radiation (FPAR), and meteorological information from Modern-Era Retrospective analysis for Research and Applications, Version 2, (MERRA-2)[39]. This global monthly GPP is produced at a 1/12° spatial resolution and covers 1982-2016. GLASS GPP is produced using a model of LUE, which is driven by four variables and was found to be able to accurately estimate the spatial and temporal dynamics of GPP[40]. This data set covers the period 1982–2018 and is provided with an 8-d temporal resolution and a 0.05° spatial resolution. We used.

SIF is considered a more direct indicator of plant photosynthesis (GPP)[44]. The GOSIF GPP data set was produced from SIF data from Orbiting Carbon Observatory-2 (OCO-2), data for terrestrial surface vegetation and temperature from Moderate Resolution Imaging Spectroradiometer (MODIS), and MERRA-2 meteorological reanalysis data[41]. These 8-d GPP data cover 2001 to 2020 with a 0.05° spatial resolution. FLUXNET GPP data consist of globally distributed eddy-covariance observations of fluxes of carbon and energy. Eddy covariance fluxes of FLUXNET and climate data were used to derive FLUXCOM GPP by upscaling methods (machine learning)[43]. Seasonal variations in the FLUXCOM data set were found to be consistent with atmospheric inversion-based carbon fluxes[43]. This monthly GPP data set covers 2001 to 2015 and is provided at a 1/12° spatial resolution. Daily FLUXSAT GPP data set provided at 0.05° spatial resolution was produced by training a neural network with FLUXNET 2015 eddy covariance tower sites data and MODIS reflectance data from 2000 to 2020[45,46].

All of the above GPP and vegetation index data sets were resampled to 0.1° using cubic convolution interpolation to match the spatial resolution of the temperature data set. The maximum-value composite (MVC) method[47] was applied to produce all GPP and vegetation index data sets as monthly observations to match the temporal resolution of the temperature data set.

FLUXNET 2015 observations

We used flux-tower (FLUXNET2015) based GPP and air temperature to calculate the optimal temperature. The FLUXNET2015 dataset provides measurements of CO_2, water, and energy exchange between the biosphere and the atmosphere, and other meteorological measurements (e.g., air temperature), from 212 sites around the globe, covering the periods before 2015[48]. The sites having more than 10 years of daily observations of GPP and temperature during 2001–2014 were chosen for the analysis (34 sites, Supplementary Table 2). We estimated the optimal temperature for two different 5-year periods: 2001–2005 and 2010–2014 (It should be noted that the observations at some sites might not be available in 2001–2002 or 2013–2014, and observations in 2003–2007 or 2008–2012 were used as alternatives). We also excluded the sites with a failure to capture the optima temperature.

Climatic data

To estimate the robustness of the extraction of T_{opt}, we used two data sets of monthly mean temperature (T_{mean}) to derive the optimal temperature ($\mathbf{T}_{opt}^{mean}$) based on mean temperatures: CRU TS (Climatic Research Unit gridded Time Series) and ERA5. The ERA5 data set of monthly T_{mean} with a 0.1° spatial resolution was produced by the Copernicus Climate Change Service at the European Centre for Medium-Range Weather Forecasts (ECMWF). The data set is the fifth generation reanalysis of data for the global climate (ERA5-land)[49]. The CRU monthly T_{mean} is derived from an extensive network of observations from meteorological stations gridded at 0.5° spatial resolution from the period 1901–2020[50]. We used T_{opt}^{mean} as basis for the optimal temperature (T_{opt}). Daily maximum temperature, however, is also important for the thermal acclimation of vegetation. We therefore also used the monthly means in the ERA5 data set of daily maximum temperatures (T_{max}) to derive the optimal temperature ($\mathbf{T}_{opt}^{max}$) and compared it with $\mathbf{T}_{opt}^{mean}$ (Supplementary Fig. 20). The monthly mean ERA5 T_{max} was derived from hourly ERA5 temperatures with a 0.1° spatial resolution. We averaged T_{max} to into a monthly data set to match the spatiotemporal resolution of the ERA5 monthly mean temperature.

CMIP6 data sets

We used data for GPP and temperature from 23 Earth system models (ESMs) (Supplementary Table 4) in Phase 6 of the Coupled Model Intercomparison Project (CMIP6) to produce the projected T_{opt}. The scenarios used in CMIP6 combine Shared Socioeconomic Pathways (SSPs) and targeted radiative forcing levels for the end of the 21st century[51]. SSP126, SSP245, SSP370, and SSP585 represent various emissions of CO_2 from the lowest to the highest level[51]. We used data sets of monthly GPP and temperature for 2017 to 2100 under different scenarios (SSP126, SSP245, SSP370, and SSP585) to derive the projected changes in T_{opt}.

Other auxiliary data sets

Global climatic zones. The current map of climatic zones is an improved map of the Köppen-Geiger classification of climate with a 1/12° spatial resolution (Supplementary Fig. 21). Multiple independent data sources have been used to maximize the accuracy of the classification of climatic zones[52].

ESA CCI land cover. We used the ESA climate change initiative (CCI) land-cover map for 2000[53] with a spatial resolution of 300 m to derive masks of irrigated cropland and areas with sparse or no vegetation. The masked areas were: irrigated cropland, barren land, permanent snow, and ice-covered areas (Supplementary Fig. 21).

These auxiliary data sets were resampled to 1° using nearest-neighbour interpolation to match the spatial resolution of the T_{opt} data.

Analysis

Extraction of T_{opt}. We followed the basic concept of a previously suggested method[6,9] to derive T_{opt}. Unlike previous studies, however, we extracted T_{opt} by testing the relationships (response curves) between monthly GPP and monthly mean temperature (both with 1° spatial resolution) within a 5-y temporal window (12 × 5) and a 1° spatial window (10×10) (different spatio-temporal windows were also tested) (Supplementary Fig. 3) to secure enough observations for a statistically robust extraction of T_{opt}. GPP and its corresponding T within a spatio-temporal window were grouped into multiple bins by intervals of 0.5 °C. We used the 90% quantiles of GPP and T as the response of GPP to T for each bin, because other factors (e.g. residual cloud cover, sun-sensor viewing angle configuration and extreme climatic events) may also affect GPP. The Savitzky-Golay filter[54] was then used to smooth the response curve to reduce data noise. T_{opt} for the five years was defined as the T at which the corresponding GPP was at its maximum along the smoothed response curve (Supplementary Fig. 1). Areas from where T_{opt} was extracted at the end of the curve were considered as areas of unsuccessful extractions, as a maximum could not be established (Supplementary Fig. 1d). For areas where T_{opt} was successfully extracted, < 60% of all years were excluded. Masks were applied to exclude irrigated cropland and areas with sparse or no vegetation (Supplementary Fig. 21b).

Model simulations

TRENDY. To study the drivers of the changing T_{opt}, we used six vegetation models (ISAM, LPJ-GUESS, LPX-Bern, ORCHIDEE, ORCHIDEEv3, and VISIT) for simulating monthly GPP at 0.5° spatial resolution during 1982 to 2016 under different conditions (Supplementary Table 3). GPP datasets from these models are based on photosynthetic light-response curves with different factors, including light level, leaf-internal CO2 concentration (so adjusted for stomatal response), water, nitrogen, phosphorus and temperature[55,56]. It should be noted that the short-term responses of vegetation to environmental factors have already been included in the land models, but long-term responses (i.e., thermal acclimation at leaf level) is not included. However, changes in the plant function type (PFT) have already been included in these models, which may lead to different T_{opt} because the temperature ranges for optimal photosynthesis differ per PFT composition[57,58]. These models were driven by historical changes in three factors (atmospheric CO_2, climate, and land

cover)[13]. Specifically, under Scenario 0 (S0), all of the above factors are set as constant values (using the monthly recycling mean and variability of factors from 1901 to 1920 in the following periods: 1921–1940, 1941-1960, 1961-1980, 1981-2000, and 2000-2020). Scenario 1 (S1) was driven by varying atmospheric CO_2, but constant climate and land cover. Scenario 2 (S2) was driven by varying atmospheric CO_2 and climate, but constant land cover. Scenario 3 (S3) was driven by varying atmospheric CO_2, climate, and land cover. We extracted T_{opt} using a 5-y temporal window and a spatial window of 5×5 grid cells under all scenarios. The difference of changes in T_{opt} between S1 and S0 (S1-S0) was then used to estimate the impact of CO_2 on T_{opt}. Similarly, S2-S1 and S3-S2 indicate the impact of climate change and land cover change, respectively (Fig. 2A). We used a different spatial window size (5×5) than for the extraction of T_{opt} from satellite data sets, because of the relatively coarse spatial resolution of the forcing data used as input for the model. The importance of the size of the spatial window was tested and was found to have only a minor impact on the extraction of T_{opt} (Supplementary Fig. 3).

LPJ-GUESS. Climate variables including temperature, precipitation, and solar radiation were combined into one variable in the TRENDY models, which impedes a quantification of the contribution of individual climate variables. We thus applied the Lund-Potsdam-Jena General Ecosystem Simulator (LPJ-GUESS) model[59], forced by individual climate variables (temperature, precipitation, solar radiation, nitrogen deposition, and CO2), for simulating monthly GPP at 0.5° spatial resolution for the period 1982 to 2016. Global monthly atmospheric CO_2 levels and historical monthly CRU climatic data sets (temperature, precipitation, radiation) at 0.5° spatial resolution from 1901 to 2020 were used to drive the model. In addition to the variables used to force the TRENDY models, we also included nitrogen deposition as a variable, which is an important factor for ecosystem photosynthesis. Firstly, model runs were forced with all factors varying (temperature, precipitation, solar radiation, CO_2 level, and nitrogen deposition) under standard conditions (ALL) to simulate monthly GPP. Secondly, similar to the TRENDY simulations, the LPJ-GUESS model was forced with one varying factor while the remaining factors were kept constant (monthly recycling mean and variability from 1901 to 1920). Thirdly, the model-simulated GPP data sets were used to extract T_{opt} with a 5-year temporal window and a spatial window of 5×5 grid cells under different conditions to evaluate the contribution of each forcing variables to the changing T_{opt} (Fig. 2B).

Trend analysis. The Theil-Sen estimator and a Mann-Kendall trend test were used at the pixel level to assess historical (1982–2016) and projected (2017–2100) trends in T_{opt}. Yue-Pilon prewhitening method was used to remove serial autocorrelations[60] in time series of T_{opt} which was calculated with a moving window. The significance level of $p < 0.05$ was applied to retain clear and coherent spatial clusters/patterns of trends. The Mann-Kendall trend test is a non-parametric test, which is robust against outliers and does not require the data to be normally distributed.

Relative importance analysis. We used a relative weight analysis approach[61] to estimate to what extent the trend in T_{opt} can be explained by the climatic factors. The relative importance is assessed using the "lmg" approach in a multiple regression[62], where the trend in T_{opt} is set as response variable and trends in temperature, precipitation and radiation as explanatory variables.

Data availability

All data used to support the findings of this study are publicly available. The data used to generate figures are available through figshare (https://figshare.com/articles/dataset/dataset_rar/26340871). NIR GPP data are available from https://figshare.com/articles/dataset/Long-term_1982-2018_global_gross_primary_production_dataset_based_on_NIRv/12981977/2. Improved LUE GPP data are available from https://daac.ornl.gov/cgi-bin/dsviewer.pl?ds_id=1789. GLASS GPP data are available from http://www.glass.umd.edu/Download.html. GOSIF GPP data are available from https://globalecology.unh.edu/data/GOSIF.html. FLUXCOM GPP data are available from https://www.bgc-jena.mpg.de/geodb/projects/Home.php. FLUXSAT GPP data are available from https://daac.ornl.gov/VEGETATION/guides/FluxSat_GPP_FPAR.html. GIMMS NDVI data are available from https://climatedataguide.ucar.edu/climate-data/ndvi-normalized-difference-vegetation-index-3rd-generation-nasagfsc-gimms. GIMMS LAI data are available from https://zenodo.org/records/8281930. MOD13C2 NDVI, EVI, and reflectance data are available from https://search.earthdata.nasa.gov/search. ERA5 climatic data are available from https://www.ecmwf.int/en/forecasts/datasets/reanalysis-datasets/era5. CRU climatic data are available from https://crudata.uea.ac.uk/cru/data/hrg/. CMIP6 outputs are available from https://esgf-node.llnl.gov/search/cmip6/. Köppen-Geiger climate classification is available from: http://www.gloh2o.org/koppen/. ESA CCI land cover data are available from https://www.esa-landcover-cci.org/. TRENDY model simulations are available from Hui Yang (huiyang.pku@gmail.com) upon request. LPJ-GUESS model simulations are available from Guy Schurgers (gusc@ign.ku.dk) upon request.

Code availability

Python code for processing the data and generating the figures are available from the corresponding author upon request.

Received: 11 February 2024; Accepted: 20 August 2024;
Published online: 28 August 2024

References

1. Friedlingstein, P. et al. Global Carbon Budget 2021. *Earth Syst. Sci. Data* **14**, 1917–2005 (2022).
2. Lloyd, J. & Farquhar, G. D. Effects of rising temperatures and [CO2] on the physiology of tropical forest trees. *Philos. Trans. R. Soc. Lond. B Biol. Sci.* **363**, 1811–1817, (2008).
3. Kattge, J. & Knorr, W. Temperature acclimation in a biochemical model of photosynthesis: a reanalysis of data from 36 species. *Plant Cell Environ.* **30**, 1176–1190 (2007).
4. Medlyn, B. et al. Temperature response of parameters of a biochemically based model of photosynthesis. *Ii. A Rev. Exp. data.* **25**, 1167–1179 (2002).
5. Berry, J. & Bjorkman, O. Photosynthetic response and adaptation to temperature in higher plants. *Annu. Rev. Plant Physiol.* **31**, 491–543 (1980).
6. Huang, M. et al. Air temperature optima of vegetation productivity across global biomes. *Nat. Ecol. Evol.* **3**, 772–779 (2019).
7. Luo, Q. Temperature thresholds and crop production: a review. *Clim. Change* **109**, 583–598 (2011).
8. Bennett, A. C. et al. Thermal optima of gross primary productivity are closely aligned with mean air temperatures across Australian wooded ecosystems. *Glob. change Biol.* **27**, 4727–4744 (2021).
9. Niu, S. et al. Thermal optimality of net ecosystem exchange of carbon dioxide and underlying mechanisms. *N. phytologist* **194**, 775–783 (2012).
10. Chen, A., Huang, L., Liu, Q. & Piao, S. Optimal temperature of vegetation productivity and its linkage with climate and elevation on the Tibetan Plateau. *Glob. change Biol.* **27**, 1942–1951 (2021).
11. Kumarathunge, D. P. et al. Acclimation and adaptation components of the temperature dependence of plant photosynthesis at the global scale. *N. phytologist* **222**, 768–784 (2019).
12. Wang, B. et al. Dryness controls temperature-optimized gross primary productivity across vegetation types. *Agric. For. Meteorol.* **323**, 109073 (2022).
13. Zhu, Z. et al. Greening of the Earth and its drivers. *Nat. Clim. change* **6**, 791–795 (2016).

14. Way, D. A. Just the right temperature. *Nat. Ecol. Evol.* **3**, 718–719 (2019).
15. Piao et al. Characteristics, drivers and feedbacks of global greening. *Nat. Rev. Earth Environ.* **1**, 14–27 (2019).
16. Jong, R., Verbesselt, J., Schaepman, M. E. & Bruin, S. Trend changes in global greening and browning: contribution of short-term trends to longer-term change. *Glob. change Biol.* **18**, 642–655 (2012).
17. Tian, F. et al. Evaluating temporal consistency of long-term global NDVI datasets for trend analysis. *Remote Sens. Environ.* **163**, 326–340 (2015).
18. Lucht, W. et al. Climatic control of the high-latitude vegetation greening trend and Pinatubo effect. *Science*. **296**, 1687–1689 (2002).
19. Yuan, W. et al. Thermal adaptation of net ecosystem exchange. *Biogeosciences* **8**, 1453–1463 (2011).
20. Xia, J. et al. Terrestrial carbon cycle affected by non-uniform climate warming. *Nature Geosci.* **7**, 173–180 (2014).
21. Sage, R. F. & Kubien, D. S. The temperature response of C3 and C4 photosynthesis. *Plant, cell Environ.* **30**, 1086–1106 (2007).
22. Ficklin, D. L. & Novick, K. A. Historic and projected changes in vapor pressure deficit suggest a continental-scale drying of the United States atmosphere. *J. Geophys. Res.: Atmos.* **122**, 2061–2079 (2017).
23. Grossiord, C. et al. Plant responses to rising vapor pressure deficit. *N. phytologist* **226**, 1550–1566 (2020).
24. Pearson, R. G. et al. Shifts in Arctic vegetation and associated feedbacks under climate change. *Nat. Clim. change* **3**, 673–677 (2013).
25. Wang, J. A. et al. Extensive land cover change across Arctic-Boreal Northwestern North America from disturbance and climate forcing. *Glob. change Biol.* **26**, 807–822 (2020).
26. Carnicer, J., Barbeta, A., Sperlich, D., Coll, M. & Penuelas, J. Contrasting trait syndromes in angiosperms and conifers are associated with different responses of tree growth to temperature on a large scale. *Front Plant Sci.* **4**, 409 (2013).
27. Reich, P. B. et al. Effects of climate warming on photosynthesis in boreal tree species depend on soil moisture. *Nature* **562**, 263–267 (2018).
28. Rodrigues, W. P. et al. Long-term elevated air [CO 2] strengthens photosynthetic functioning and mitigates the impact of supra-optimal temperatures in tropical Coffea arabica and C. *canephora species* **22**, 415–431 (2016).
29. Taub, D. R., Seemann, J. R. & Coleman, J. S. J. P. Cell & Environment. *Growth elevated CO2 Prot. photosynthesis high-temperature damage* **23**, 649–656 (2000).
30. Fensholt, R. & Proud, S. R. Evaluation of Earth Observation based global long term vegetation trends — Comparing GIMMS and MODIS global NDVI time series. *Remote Sens. Environ.* **119**, 131–147 (2012).
31. Zhang, Y. et al. Future reversal of warming-enhanced vegetation productivity in the Northern Hemisphere. *Nat. Clim. Change* **12**, 581–586 (2022).
32. Keenan, T. F. & Riley, W. J. Greening of the land surface in the world's cold regions consistent with recent warming. *Nat. Clim. change* **8**, 825–828 (2018).
33. Duffy, K. A. et al. How close are we to the temperature tipping point of the terrestrial biosphere? *Sci. Adv.* **7**, eaay1052 (2021).
34. Baldocchi, D. D. et al. Outgoing Near-Infrared Radiation From Vegetation Scales With Canopy Photosynthesis Across a Spectrum of Function, Structure, Physiological Capacity, and Weather. *J Geophys. Res.: Biogeosci.* **125**, https://doi.org/10.1029/2019jg005534 (2020).
35. Wang, Zhang, Y., Ju, W., Qiu, B. & Zhang, Z. Tracking the seasonal and inter-annual variations of global gross primary production during last four decades using satellite near-infrared reflectance data. *Sci. total Environ.* **755**, 142569 (2021).
36. Pinzon, J. & Tucker, C. A Non-Stationary 1981–2012 AVHRR NDVI3g Time Series. *Remote Sens.* **6**, 6929–6960 (2014).
37. Cao, S. et al. Spatiotemporally consistent global dataset of the GIMMS leaf area index (GIMMS LAI4g) from 1982 to 2020. *Earth Syst. Sci. Data* **15**, 4877–4899 (2023).
38. Camps-Valls, G. et al. A unified vegetation index for quantifying the terrestrial biosphere. *Sci Adv*. **7**, eabc7447 (2021).
39. Madani, N. & Parazoo, N. Global Monthly GPP from an Improved Light Use Efficiency Model, 1982-2016. *ORNL DAAC,* https://doi.org/10.3334/ORNLDAAC/1789 (2020).
40. Yuan, W. et al. Global estimates of evapotranspiration and gross primary production based on MODIS and global meteorology data. *Remote Sens. Environ.* **114**, 1416–1431 (2010).
41. Li, X. & Xiao, J. A Global, 0.05-Degree Product of Solar-Induced Chlorophyll Fluorescence Derived from OCO-2, MODIS, and Reanalysis Data. *Remote Sens.* **11**, 517 (2019).
42. Zhang, Y., Joiner, J., Alemohammad, S. H., Zhou, S. & Gentine, P. J. B. A global spatially contiguous solar-induced fluorescence (CSIF) dataset using neural networks. *Biogeosciences.* **15**, 5779–5800 (2018).
43. Tramontana, G. et al. Predicting carbon dioxide and energy fluxes across global FLUXNET sites with regression algorithms. *Biogeosciences* **13**, 4291–4313 (2016).
44. Meroni, M. et al. Remote sensing of solar-induced chlorophyll fluorescence: Review of methods and applications. *Remote Sens. Environ.* **113**, 2037–2051 (2009).
45. Joiner, J. *et al*. Estimation of Terrestrial Global Gross Primary Production (GPP) with Satellite Data-Driven Models and Eddy Covariance Flux Data. *Remote Sensing* **10**, https://doi.org/10.3390/rs10091346 (2018).
46. Joiner, J. & Yoshida, Y. Satellite-based reflectances capture large fraction of variability in global gross primary production (GPP) at weekly time scales. *Agricultural and Forest Meteorology* **291**, https://doi.org/10.1016/j.agrformet.2020.108092 (2020).
47. Holben, B. N. Characteristics of maximum-value composite images from temporal AVHRR data. *Int. J. remote Sens.* **7**, 1417–1434 (1986).
48. Pastorello, G. et al. The FLUXNET2015 dataset and the ONEFlux processing pipeline for eddy covariance data. *Sci Data.* **7**, 225 (2020).
49. Muñoz-Sabater, J. et al. ERA5-Land: A state-of-the-art global reanalysis dataset for land applications. *Earth Syst Sci Data.* **13**, 4349–4383 (2021).
50. Harris, I., Osborn, T. J., Jones, P. & Lister, D. Version 4 of the CRU TS monthly high-resolution gridded multivariate climate dataset. *Sci. data* **7**, 109 (2020).
51. Gidden, M. J. et al. Global emissions pathways under different socioeconomic scenarios for use in CMIP6: a dataset of harmonized emissions trajectories through the end of the century. *Geoscientific Model Dev.* **12**, 1443–1475 (2019).
52. Beck, H. E. et al. Present and future Koppen-Geiger climate classification maps at 1-km resolution. *Sci. data* **5**, 180214 (2018).
53. Defourny, P. et al. Accuracy assessment of a 300 m global land cover map: The GlobCover experience. https://publications.jrc.ec.europa.eu/repository/handle/JRC54524 (2009).
54. Savitzky, A. & Golay, M. J. J. A. C. Smoothing and differentiation of data by simplified least squares procedures. *Analytical chemistry*. **36**, 1627–1639 (1964).
55. Haxeltine, A. & Prentice, I. J. F. E. A general model for the light-use efficiency of primary production. *Functional Ecology*. **10**, 551–561 (1996).
56. Smith, B. et al. Implications of incorporating N cycling and N limitations on primary production in an individual-based dynamic vegetation model. *Biogeosciences*. **11**, 2027–2054 (2014).
57. Niinemets, Ü. J. P. R. Variation in leaf photosynthetic capacity within plant canopies: optimization, structural, and physiological constraints and inefficiencies. *Photosynth Res.* **158**, 131–149 (2023).
58. Kanta, C., Kumar, A., Chauhan, A., Singh, H. & Sharma, I. P. in Plant Functional Traits for Improving Productivity 41–58 (Springer, 2024).

59. Smith, B., Prentice, I. C. & Sykes, M. T. Representation of vegetation dynamics in the modelling of terrestrial ecosystems: comparing two contrasting approaches within European climate space. *Glob. Ecol. Biogeogr.* **10**, 621–637 (2001).
60. Yue, S. & Wang, C. Y. Applicability of prewhitening to eliminate the influence of serial correlation on the Mann-Kendall test. *Water Resour. Res.* **38**, 4-1–4-7 (2002).
61. Tonidandel, S. & LeBreton, J. M. Relative Importance Analysis: A Useful Supplement to Regression Analysis. *J. Bus. Psychol.* **26**, 1–9 (2011).
62. Grömping, U. J. T. A. S. Estimators of relative importance in linear regression based on variance decomposition. *Am. Stat*. **61**, 139–147 (2007).

Acknowledgements

Z.X.F. is funded by the China Scholarship Council (CSC) (Grant 201906410082). W.M.Z. and M.B. are supported by ERC project TOFDRY (Grant 947757). L.W. considers this work a contribution to his Carlsberg Foundation Internationalization Fellowship project (grant CF21-0157). R.F. acknowledge support by the Villum Foundation through the project "Deep Learning and Remote Sensing for Unlocking Global Ecosystem Resource Dynamics". (DeReEco) (Project Number 34306).

Author contributions

Z.X.F., W.M.Z., and R.F. conceived the study. Z.X.F. conducted data analysis and wrote the first draft of manuscript. L.H.W., G.S., P.C., M.B., and R.F. aided in the discussion of the results. G.S. and H.Y. aided in the simulations of TRENDY and LPJ-GUESS under different scenarios. Z.X.F., W.M.Z., L.H.W., G.S., P.C., J.P., R.F., K.H., Q.S. and M.B. contributed to the interpretation of the results and to the text.

Competing interests

The authors declare no competing interests.

Additional information

Supplementary information The online version contains supplementary material available at https://doi.org/10.1038/s43247-024-01636-9.

Correspondence and requests for materials should be addressed to Wenmin Zhang.

Peer review information *Communications Earth & Environment* thanks Dushan P. Kumarathunge and Mirindi Eric Dusenge for their contribution to the peer review of this work. Primary Handling Editors: Alireza Bahadori and Aliénor Lavergne. A peer review file is available.